Local electrical properties of thermally grown oxide films formed on duplex stainless steel surfaces

Liqiu Guo[a], Binjie Yang[a], Jianying He[b], Lijie Qiao[a]

[a] Corrosion and Protection Center, Key Laboratory for Environmental Fracture (MOE), University of Science and Technology Beijing, Beijing 100083, China

[b] Department of Structural Engineering, Norwegian University of Science and Technology, 7491, Trondheim, Norway

Abstract The electrical properties and chemical compositions of oxide films formed on duplex stainless steel (DSS 2507) at different temperatures were investigated by using Current Sensing Atomic Force Microscopy (CSAFM), X-ray Photoelectron Spectroscopy (XPS) and Auger Electron Spectroscopy (AES). The results showed that continuous chromium-rich structure extended to the oxide film surface and duplex structure for inner chromium-rich layer and outer iron-rich layer. The conductivity of oxide films was closely linked to the thickness and film structures, which associated with thermodynamics and kinetics process of film growth at different temperature. The corresponding semiconductor band structures of the oxide films formed on austenite and ferrite phases at different temperature were evaluated, further verifying the Cr element in passive film played a positive effect on resistance to corrosion from the perspective of oxide semiconductor conductivity.

***Keywords*:** Semiconductor; CSAFM; Oxide film; DSS; XPS; AES

1. Introduction

Passive films and oxide films formed on the surface of stainless steel and iron are closely related to the corrosion of the stainless steel [1-5]. Local corrosion including pitting corrosion, intergranular corrosion and stress corrosion usually occurs on a stainless steel surface [2-5], along with rupture of passive film or oxide film [2, 4, 6]. The electrical properties of passive films and oxide films are significant for the study of corrosion, which is an electrochemical process.

The chemical compositions of the passive films and oxide films are mainly oxides, hydroxides and hydrates of alloys [7-10], and the films usually consist of a bilayer structure, inner chromium-rich layer and outer iron-rich layer [11-16]. Thickness of passive films and oxide films ranges from several to tens of nanometers due to the different growth conditions [11, 12, 17]. Stainless steel surface films possess semiconductor characters, determined by relative abundances of metal oxides, hydroxides and hydrates [5, 11, 16, 18], because these metal oxides, hydroxides and hydrates show different semiconductor characters of p-type and n-type. For example, Cr_2O_3, FeO, NiO, MoO_2 present p-type semiconductor properties controlled by cationic vacancies, while Fe_2O_3, FeOOH, CrO_3, MoO_3 are n-type caused by oxygen vacancies and metal atoms clearances [14, 19-22]. $Cr(OH)_3$ presents different p-n characteristics depending on the growth conditions [23].

The electrical properties of passive films and oxide films formed on stainless steel are closely connected with chemical composition, structure, thickness, depth distribution, external environment, and so on [9, 11-14, 18]. Mott-Schottky and photoelectron-chemistry analyses are commonly used to study the electrical properties

of stainless steel surface films [11, 16, 18, 24-28]. In the Mott-Schottky plots, surface films show different semiconductor characters under different scanning potential because of typical bilayer structure [11, 13, 16, 24]. Cr_2O_3 in the inner present p-type and outer Fe_2O_3 present n-type semiconductor properties [11, 13, 16]. However, n-type bilayer structure has also been reported [24]. The main drawback of Mott-Schottky and photoelectron-chemical analyses is that they can't be applied in micro scale.

Current Sensing Atomic Force Microscopy (CSAFM) is an effective method to study the electrical properties of surface films on stainless steel in micro scale [29]. Duplex phases of duplex stainless steel can easily be distinguished by MFM. Souier et al. employed CSAFM to study the electrical property aging of oxide film on duplex stainless steel (DSS) formed in air [30]. By same method Guo et al. investigated the electrical properties of passive film under different passive potentials in borate buffer solution [9], and Lin et al. discovered electromechanical coupling phenomenon of oxide films formed on DSS at 300°C [31]. However, there are divergences of electrical properties of surface films formed on DSS in the few CSAFM researches, and the study on the difference between electrical properties of duplex phases is still insufficient .

The present work aims to investigate the influence of temperature on electrical properties of oxide films formed on DSS by using CSAFM, combining with X-ray photoelectron spectroscopy (XPS) and Auger electron spectroscopy (AES) for characterization of chemical composition and element depth distribution of oxide films.

2. Experimental procedure

2.1. Materials and samples preparation

Conventional 2507 DSS was used because of the distinct phases described in previous reports [9]. The specimens were mechanically polished with SiC paper up to 2000 grit and diamond paste sized of 1.5 μm; then electrochemically polished in a mixed solution of HNO_3:H_2O = 1:1 for 30s at 1.2 V applied voltage; and finally cleaned with ethanol in an ultrasonic bath and dried in N_2 gas flow. In order to record the observing position, indentation marks on the sample surface were made by a digital micro-hardness tester, HVS-1000.

The 2507 DSS samples were held in air at room temperature (RT) for 24 h to form stable oxide films, and then put in a resistance furnace for 30 min at 300°C and 400°C to obtain thicker and denser oxidation films.

2.2. CSAFM and MFM measurements

The CSAFM measurements of oxide films were carried out using Agilent 5500 AFM (Agilent Technologies, USA) operated in the current sensing mode. The CSAFM operation was in air environment and relative humidity of about 25%. A surface region with 80 μm × 80 μm was scanned at a frequency of 0.1 Hz. The probes used were SCM-PIC conductive Cr-coated silicon tips with a force constant of 0.2 N/m and sensitivity coefficient of 242 nm/V. Current values in duplex phases were calculated by averaging three 100 μm^2 (10 μm × 10μm) areas in each phase in every CSAFM image using the commercial software PicoView 1.8. The magnetic force microscopy (MFM) measurement was carried out using a Dimension AFM (Nanoscope V, Veeco

Instruments Inc.) with NANOSENSORS™ PPP-MFMR hard magnetic material coated probes (2.8 N/m force constant and 45–115 kHz resonant frequency). The principle and details of CSAFM and MFM measurements were described in the previous reports [9, 29, 31].

2.3. Surface analysis

The chemical composition within 5 nm surface of the oxide films was investigated with XPS using a scanning X-ray Microprobe^{TM} instrument (PHI Quantera SXM^{TM}, ULVAC-PHI, Japan). The curve fitting was performed using the commercial software XPS Peak, version 4.1 with Shirley background subtraction and Gaussian–Lorentzian tail functions, to obtain better spectra fitting.

The element distribution in depth of the oxide films was analyzed by AES using a nano scanning auger system (model PHI-700, ULVAC-PHI, Japan) based on the Chinese standard GB/T 26533-2011. Auger test was carried out by coaxial electron gun and CMA energy analyzer with high voltage of electron gun 5KV, energy resolution 1‰ and incident Angle 30°. The vacuum degree was controlled above 3.9×10^{-9} Torr. The sputtering used a scanning type Ar gun, and the prototype was the thermal oxidation SiO_2/Si with the sputtering rate 5.0 nm/min.

3. Results

3.1. CSAFM and MFM measurements of the oxide films

Fig. 1 and Fig. 2 show the CSAFM and MFM images of the oxide films obtained

at 300°C and 400°C, respectively. The identification of austenite (γ) and ferrite (α) phases in the topography images (Fig. 1a and Fig. 2a) is proven by MFM images (Fig. 1b and Fig. 2b), where striped magnetic domains can be observed in the region of ferromagnetic ferrite, but not in the paramagnetic austenite. It is observed that the higher austenite grains disperse on the lower ferrite matrix, in consistent with previous literature reports [9, 29, 31].

The corresponding current maps of oxide film formed at 300°C are shown in Fig. 1c to 1f. The tip load is 84.7 nN, where the calculation method refers to previous works [31]. The current value increases with voltage rising from 1 V to 5 V. The austenitic current is always higher than that in ferrite phase, indicated by the brighter austenite phase than ferrite phase in Fig. 1c to 1f. Lin et al. have found similar phenomenon in the passive films and oxide films of DSS [9, 29, 31].

The current maps of oxide film formed at 400°C in Fig. 2c to 2f show a turnover of current in duplex phases with increasing voltage from 1 V to 5 V. With the sample bias of 1 V the austenite phase current is higher than that in ferrite phase. When increasing the sample bias to 2V, the current values in austenite are comparable with that in ferrite. In the case of 4 V and 5 V, the current in ferrite become more brighter than those in austenite, similar with Souier's research [30]. Eventually current value in ferrite goes beyond that in austenite, and current reversal phenomenon occurs.

The average current values of austenite and ferrite phases at different scan voltages are listed in Table 1. As the sample bias increases from 1 V to 5 V, currents in both phases increase, while the relative differences of duplex phases current decreases. In

the case of 300°C, the ratios of average current values in austenite to ferrite (A/F) are 743.7, 211.6 and 190.6 with the sample bias of 2 V, 4 V and 5 V, suggesting that Current signal in austenitic phase is two orders of magnitude higher than that in ferrite phase at 300°C, consistent with Fig. 1c to 1f. The A/F ratios for the oxide films at 400°C are 2.1, 1.0, 0.8 and 0.3, shows that the current signals of austenite and ferrite phases are in the same order of magnitude and finally the ferrite phase presents slight better conductivity with the sample bias increased to 4 V.

3.2. AES depth analysis of the oxidation films

The chemical composition in depth profiles are plotted in Fig. 3. From auger depth profile in Fig. 3, movements in the depth of different elements in the austenite and ferrite phases can be observed, in accordance with previous reports [11-15]. The oxide film thickness can be identified by the intersection of oxygen and iron lines in the plots. This means that the film thickness is around 18 nm in austenitic and 32 nm in ferrite at 300°C, and the values increase to 34 nm and 38 nm at 400°C. Depth profiles of Cr/Fe atomic ratio in Fig. 3c and 3f show different structures of the oxide films formed in duplex phases at two temperatures. In the oxide film formed at 300°C in Fig. 3c, the austenite phase possesses an inner chromium-rich layer and an outer iron-rich layer and the thickness of each layer is about 10 nm. But the ferrite phase display a continuous chromium-rich layer from inside to the outside surface with outer higher chromium-rich layer about 20 nm than inner chromium-rich layer about 10nm，which can be regarded as a duplex chromium-rich structure. For the oxide film formed

at 400°C in Fig. 3f, austenite and ferrite phases show similar film structure but larger film thickness compared with the austenite phase oxide film formed at 300°C. Each layer in both phases is near 20 nm.

Element Cr is more easily oxidized to Cr_2O_3 than Fe to Fe_2O_3 because of the lower energy needed to generate on the thermodynamics [10]. But In the aspect of dynamics element Fe is easier to diffuse outside the layer of oxide film than Cr under the right conditions such as higher temperature [33,34]. The differences in thermodynamic caused the different film structures of austenite and ferrite phases formed at different temperature. Duplex structure discovered in oxide films formed in austenite phase at 300°C (Fig. 3c) and in both phases at 400°C (Fig. 3f). Outer iron-rich layer can be attributed to the fast diffusion of iron kinetically [10, 33, 34]. If there is no better dynamic conditions meeting the diffusion of Fe, Cr_2O_3 will grow through the whole oxide film thermally [10, 34], just like the ferrite phase oxide film formed at 300°C (Fig. 3c). Higher content of substances containing element Cr in oxide film formed at 300°C than 400°C in the statistical by XPS (Table.3) should be associated with the continuous rich chromium layer in the ferrite phase at 300°C. Outer iron-rich layer existing in ferrite phase oxide film formed at 400°C but not at 300°C can be attributed to satisfactory diffusion conditions at higher temperature 400°C [10, 33, 34]. Moreover, the slightly declined Cr/Fe peak in outer iron-rich layer in austenite phase at 400°C is caused by the similar reason. In the oxide layer, the higher value of Cr/Fe in ferrite than in austenite at same temperatures is associated with higher chromium content in ferrite phase [9]. Thermodynamic differences of element Fe and Cr oxide

formation in oxide films lead to different film structures and thicknesses [10, 33, 34].

3.2. XPS analysis of oxidation films

Chemical compositions in only 5 nm thickness from the surface are analyzed by XPS, which is situated just outside the surface of the oxide film with thickness about 20 nm ~ 40 nm. XPS spectra of the oxide films are shown in Fig. 4-7, and the corresponding binding energies obtained from spectra deconvolutions of the primary compounds (iron, chromium, molybdenum and nickel) in the oxide films are listed in Table 2. The Fe 2p3/2 signals in Fig. 4 illustrate the presence of three components: the bivalent (Fe2+) and two trivalent (Fe3+) species. Chemical substances containing Fe in the oxide films are mainly FeO (710.70 eV), Fe2O3 (711.50 eV) and FeOOH (712.00 eV). For the Cr 2p3/2 spectra in Fig. 5 there are three constituent peaks, representing Cr_2O_3 (576.00 eV), Cr(OH)3 (577.00 eV) and CrO3 (578.30). The Ni 2p3/2 spectra in Fig. 6 represents the metallic state (Ni, 853.30 eV), along with $Ni(OH)_2$ (856.60 eV) and NiO (855.30 eV). Mo 3d spectra in Fig. 7 indicate two kinds of six-valent Mo (Mo6+3d5/2, 232.2 eV and Mo6+3d3/2, 235.80 eV). Comparing Fig. 4a and 4b, 7a and 7b, the relative proportion of chemical substances including the same element Fe and Mo is independent of the temperature. For the substances contain element Cr, more Cr_2O_3 are detected in the oxide film formed at 400°C. In the aspect of nickel element, oxide films formed at 300°C and 400°C both contain substances of NiO and $Ni(OH)_2$, but small quantities of metal state Ni are detected at 400°C.

The percentage composition of various chemical substances is listed in Table 3,

which shows content changes in the outer surface of oxide film. The amount of substances containing element Fe dramatically rises from 42.0% to 68.3% and the amount of substances containing element Ni slightly declines from 2.9% to 2.6% as increasing oxidizing temperature from 300°C to 400°C (Table 3) are caused by the relatively higher diffusion coefficient of Fe and Ni than Cr kinetically [10, 33, 34]. Analogously, the amounts of substances containing element Cr and Mo both significantly declining respectively from 47.6% to 24.2% and from 7.5% to 4.9% should be the same reason. Substances containing element Ni and Mo take about 10.4% and 7.5% proportions in total in the outer surface of the oxide film formed at 300°C and 400°C due to their low content in the DSS about 10%.The small amount of metal state Ni only detected in oxide film formed at 400°C take a proportion of 0.3%, which should be the result of reduction during the XPS experiment [32]. The varying amounts of substances containing different elements outside the oxide films correspond to the iron-rich layer in the common duplex structure of inner chromium-rich layer and outer iron-rich layer on the stainless steel surface [11-15]. Hydroxides and hydrates usually exist in the surface of the oxide film but gradually disappear deep down in the oxide layer, with remained Fe_2O_3 and Cr_2O_3 as the main substance inside [10].

4. **Discussion**

Various oxides, hydroxyls and hydrates present different semiconductor characteristics [14, 19-23]. Besides, thickness and structure also affect the conductivity of oxide film [11-13, 18，24].

The thinner the oxide film on the stainless steel surface, the smaller the resistance is [18, 31]. Film thickness of austenitic phase formed at 300°C is below 20 nm, but film thicknesses of ferrite phase formed at 300°C and both phases formed at 400°C are all above 30 nm (Fig. 3). The lower thickness of the former is in accordance with the highest average current value as the sample bias above 1V, showed in the Table 1. Although the film thickness of the ferrite phase at 300°C is slightly thinner than that of both phases formed at 400°C, this film doesn't have a higher current value than that of both phases at 400, which can be caused by the different structures in the oxide films. In the duplex structure, oxide Fe_2O_3 and hydroxyl FeOOH outside the oxide layer formed in air are n-type semiconductors [14, 19-22] and oxide Cr_2O_3 inside the oxide layer formed in air is p-type semiconductor. While the oxide film formed on ferrite phase contain more Cr element which show p-type semiconductor.

What kind of semiconductor characteristics the oxide layer possesses are determined by the relative content of element Cr and Fe. Therefore the position in oxide layer with high Cr/Fe in depth can be analogous to p-type semiconductor layer and the position with low Cr/Fe in depth should be analogous to n-type semiconductor layer. The entire duplex structure of oxide film can be seen as different semiconductor heterojunctions [13, 16, 24]. By the Cr/Fe profile in Fig. 3e and 3f, semiconductor energy band in the semiconductor heterojunctions of oxide films can be schematically illustrated by simple models in Fig. 8. The oxide films on the austenite phase formed at 300°C and both phases formed at 400°C can be considered as a semiconductor heterojunction of inner p-type chromium-rich layer and outer n-type iron-rich layer [11-

15], as showed in Fig. 8a. The oxide film formed on ferrite phase at 300°C can be regarded as double p-type with more p-type carriers in external chromium-rich layer as in Fig. 8b. The contacts between substrate and oxide films and between oxide films and AFM probe are both schottky contacts [31].By the knowledge of semiconductor energy band, double p-type semiconductor layer has a higher p-type energy band to resist the current caused by applied positive biases to the substrate, this may lead to the relatively poor electrical performance of the oxide film in ferrite phase formed at 300°C (Fig. 1). In contrast, semiconductor heterojunction of inner p-type and outer n-type is relatively easy to carry the current through the barrier layer because of the lower n-type energy band in the outer layer [13, 16, 24], when applied positive sample biases to the substrate.

In the CSAFM experiment (Fig. 1 and 2), Prior electrical performance in oxide film of austenite phase at 300°C than 400°C showed in Table 1 may result from a decreased carrier concentration as the oxidation temperature increased [16, 18]. Comparable electrical performance in the oxide films of both phases formed at 400°C showed in Table 1 originates from the similar film thickness and energy band structure. But the current in ferrite phase increases slightly beyond that in austenite with the increased sample bias, which should be caused by the small differences in the similar semiconductor heterojunctions. Different film structures reflect varied semiconductor band structures, resulting in discrepancy in electrical performances. Because of the resistance to electric current by the chromium-rich layer which show p-type semiconductor, passive films and oxide films plays an important role in against corrosion [1, 3]. P-type semiconductor Chromium-rich layer continuous extending to

the surface in the ferrite phase oxide films formed at 300°C caused the worst electrical performance (Fig. 1 and Table 1) in the CSAFM experiment which verifying the Cr element in passive film play a positive effect on resistance to corrosion from the perspective of oxide semiconductor conductivity [2, 3, 6].

5. Conclusions

The CSAFM measurements and surface analyses (XPS and AES) are carried out to characterize the local electrical properties of oxide films on DSS formed in air at 300°C and 400°C. Chemical compositions of oxide films are temperature independent by the XPS analysis. Oxide film in the ferrite phase formed at 300°C has continuous rising chromium-rich layer extending to the surface, while oxide films in austenite phase formed at 300°C and in both phases at 400°C have a duplex structure consisting of an inner chromium-rich layer and an outer iron-rich layer. Owing to minimum thickness and heterojunction structure of inner p-type and outer n-type semiconductor, oxide films in austenite phase formed at 300°C show electrical conductivity two orders of magnitude higher than that in ferrite phase with double p-type structure. At 400°C, oxide films of both phases have the current values in the same order of magnitude due to the similar film thickness and heterojunction structure. The findings provide physical insights to the corrosion of DSS at micro scale and demonstrate that the CSAFM is an effective method to study the semiconductor properties of oxide films.

Acknowledgements

References

[1] Kruger J. Passivity of metals–a materials science perspective. International materials reviews 1988;33:113-30.

[2] Bardwell J. INFLUENCE OF THE ANODIC OXIDE FILM ON PITTING OF Fe[J]. J. A. Bardwell, J. W. Fraser, B. MacDougall, M. J. Graham, Paper, 1991 (144).

[3] Rangel CM, Silva TM, Belo MdC. Semiconductor electrochemistry approach to passivity and stress corrosion cracking susceptibility of stainless steels. Electrochimica Acta 2005;50:5076-82.

[4] Guo X Z, Gao K W, Chu W Y, et al. Correlation between passive film-induced stress and stress corrosion cracking of α-Ti in a methanol solution at various potentials[J]. Materials Science and Engineering: A, 2003, 346(1): 1-7.

[5] Ningshen S, Kamachi Mudali U, Mittal VK, Khatak HS. Semiconducting and passive film properties of nitrogen-containing type 316LN stainless steels. Corrosion Science 2007;49:481-96.

[6] Cheng Y, Luo J. Electronic structure and pitting susceptibility of passive film on carbon steel. Electrochimica Acta 1999;44:2947-57.

[7] Hara N, Sugimoto K. In Situ Analysis of Passive Films on Fe-Cr-Ni Alloy by Potential-Modulated UV-Visible Reflection Spectroscopy. Journal of the Electrochemical Society 1991;138:1594-9.

[8] Feng Z, Cheng X, Dong C, Xu L, Li X. Passivity of 316L stainless steel in borate buffer solution studied by Mott–Schottky analysis, atomic absorption spectrometry and

X-ray photoelectron spectroscopy. Corrosion Science 2010;52:3646-53.

[9] Guo LQ, Lin MC, Qiao LJ, Volinsky AA. DSS passive film electrical properties studied by in situ current sensing atomic force microscopy. Corrosion Science 2014;78:55-62.

[10] Donik Č, Kocijan A, Grant JT, Jenko M, Drenik A, Pihlar B. XPS study of DSS oxidized by oxygen atoms. Corrosion Science 2009;51:827-32.

[11] Hakiki NE, Montemor MF, Ferreira MGS, da Cunha Belo M. Semiconducting properties of thermally grown oxide films on AISI 304 stainless steel. Corrosion Science 2000;42:687-702.

[12] Olsson COA, Landolt D. Passive films on stainless steels—chemistry, structure and growth. Electrochimica Acta 2003;48:1093-104.

[13] Hakiki N, Boudin S, Rondot B, Belo MDC. The electronic structure of passive films formed on stainless steels. Corrosion Science 1995;37:1809-22.

[14] Haupt S, Strehblow H-H. A combined surface analytical and electrochemical study of the formation of passive layers on FeCr alloys in 0.5 MH 2 SO 4. Corrosion Science 1995;37:43-54.

[15] Lorang G, Belo MDC, Simoes A, Ferreira M. Chemical composition of passive films on AISI 304 stainless steel. Journal of The Electrochemical Society 1994;141:3347-56.

[16] Ferreira M, Hakiki N, Goodlet G, Faty S, Simões A, Belo MDC. Influence of the temperature of film formation on the electronic structure of oxide films formed on 304 stainless steel. Electrochimica Acta 2001;46:3767-76.

[17] Kruger J, Calvert JP. Ellipsometric-Potentiostatic Studies of Iron Passivity I. Anodic Film Growth in Slightly Basic Solutions. Journal of the Electrochemical Society 1967;114:43-9.

[18] Hakiki NE. Comparative study of structural and semiconducting properties of passive films and thermally grown oxides on AISI 304 stainless steel. Corrosion Science 2011;53:2688-99.

[19] Schultze JW, Lohrengel M. Stability, reactivity and breakdown of passive films. Problems of recent and future research. Electrochimica Acta 2000;45:2499-513.

[20] Ningshen S, Mudali UK. Hydrogen effects on pitting corrosion and semiconducting properties of nitrogen-containing type 316L stainless steel. Electrochimica Acta 2009;54:6374-82.

[21] Chuprina V, Shalya I, Karpikov I. The reactions of oxygen with the hydrogen-absorbing intermetallide TiFe. III. Phase composition of the scale formed on TiFe. Poroshk Metall 1995:82-8.

[22] Olefjord I, Wegrelius L. Surface analysis of passive state. Corrosion Science 1990;31:89-98.

[23] Kim J, Cho E, Kwon H. Photo-electrochemical analysis of passive film formed on Cr in pH 8.5 buffer solution. Electrochimica acta 2001;47:415-21.

[24] Fujimoto S, Tsuchiya H. Semiconductor properties and protective role of passive films of iron base alloys. Corrosion Science 2007;49:195-202.

[25] Ge H-H, Zhou G-D, Wu W-Q. Passivation model of 316 stainless steel in simulated cooling water and the effect of sulfide on the passive film. Applied Surface Science

2003;211:321-34.

[26] Simoes A, Ferreira M, Rondot B, da Cunha Belo M. Study of passive films formed on AISI 304 stainless steel by impedance measurements and photoelectrochemistry. Journal of the Electrochemical Society 1990;137:82-7.

[27] Cho E, Kwon H, Macdonald DD. Photoelectrochemical analysis on the passive film formed on Fe–20Cr in pH 8.5 buffer solution. Electrochimica acta 2002;47:1661-8.

[28] Di Paola A. Semiconducting properties of passive films on stainless steels. Electrochimica Acta 1989;34:203-10.

[29] Guo LQ, Lin MC, Qiao LJ, Volinsky AA. Ferrite and austenite phase identification in DSS using SPM techniques. Applied Surface Science 2013;287:499-501.

[30] Souier T, Martin F, Bataillon C, Cousty J. Local electrical characteristics of passive films formed on stainless steel surfaces by current sensing atomic force microscopy. Applied Surface Science 2010;256:2434-9.

[31] Lin MC, Wang G, Guo LQ, Qiao LJ, Volinsky AA. Electro-mechanical coupling of semiconductor film grown on stainless steel by oxidation. Applied Physics Letters 2013;103:143118.

[32] Machet A, Galtayries A, Marcus P, Combrade P, Jolivet P, Scott P. XPS study of oxides formed on nickel-base alloys in high-temperature and high-pressure water. Surface and Interface Analysis 2002;34:197-200.

[33] Allen G, Dyke J, Harris S, Morris A. A surface study of the oxidation of type 304L stainless steel at 600 K in air. Oxidation of metals 1988;29:391-408.

[34] Shibagaki S, Koga A, Shirakawa Y, Onishi H, Yokokawa H, Tanaka J. Chemical reaction path for thin film oxidation of stainless steel. Thin Solid Films 1997;303:101-6.

Table 1. Average current measured on duplex phase oxide films formed in air at 300°C and 400°C and the average current ratio of austenite to ferrite A/F .

Potential (V)	Average current (nA)					
	300 (°C)			400 (°C)		
	Austenite	Ferrite	A/F	Austenite	Ferrite	A/F
1	0.0004	0.0000	--	0.0043	0.0020	2.1
2	0.0476	0.0001	743.7	0.0055	0.0053	1.0
4	0.4020	0.0019	211.6	0.0865	0.1080	0.8
5	5.4500	0.0286	190.6	0.1600	0.4610	0.3

Table.2. Binding energy of the primary compounds in oxidation film obtained from the XPS spectra deconvolution.

Element	Peak	Species/binding energy(eV)
Fe	$2P_{2/3}$	FeO/709.90 eV; Fe_2O_3/710.90 eV; FeOOH/712.00 eV
Cr	$2P_{2/3}$	Cr_2O_3/576.00 eV; $Cr(OH)_3$/577.00 eV; CrO_3/578.30 eV
Ni	$2P_{2/3}$	Ni(met)/853.30 eV; NiO/855.30 eV; $Ni(OH)_2$/856.60 eV
Mo	$3d_{5/2}$	Mo^{6+}/232.20 eV
	$3d_{3/2}$	Mo^{6+}/235.80 eV

Table.3 Percent contents of various substances at 300°C and 400°C by XPS analysis

element	substance	Percent content	
		300(°C)	400(°C)
Fe	FeO	9.2%	19.4%
	Fe_2O_3	11.9%	18.6%
	FeOOH	20.9%	30.3%
	Total	42.0%	68.3%
Cr	Cr_2O_3	13.9%	11.0%
	$Cr(OH)_3$	28.4%	10.1%
	CrO_3	5.3%	3.1%
	Total	47.6%	24.2%
Ni	Ni	0	0.3%
	NiO	1.3%	1.2%
	$Ni(OH)_2$	1.6%	1.1%
	Total	2.9%	2.6%
Mo	$Mo^{6+}_{3d5/2}$	4.9%	3.4%
	$Mo^{6+}_{3d3/2}$	2.6%	1.5%
	Total	7.5%	4.9%

Fig.1. CSAFM and MFM measurement results of oxide film formed at 300°C. (a) AFM topography image; (b) MFM image of the same area as in (a), and the corresponding current maps with sample bias (c) +1V, (d) +2V, (e) +4V, and (f) +5V. All the current maps with the same tip normal load of 84.7 nN.

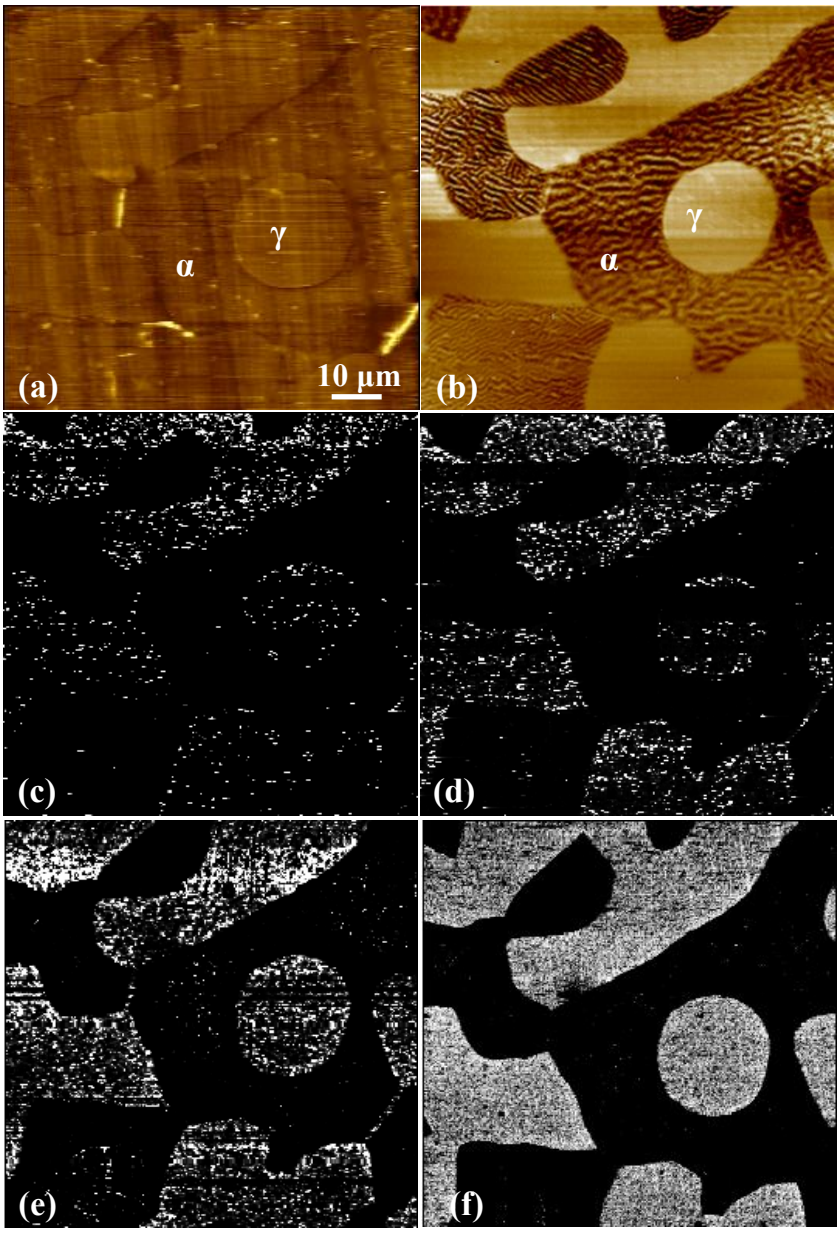

Fig.2. CSAFM and MFM measurement results of oxide film formed at 400°C. (a) AFM topography image; (b) MFM image of the same area as in (a), and the corresponding current maps with sample bias (c) +1V, (d) +2V, (e) +4V, and (f) +5V. All the current maps with the same tip normal load of 84.7 nN.

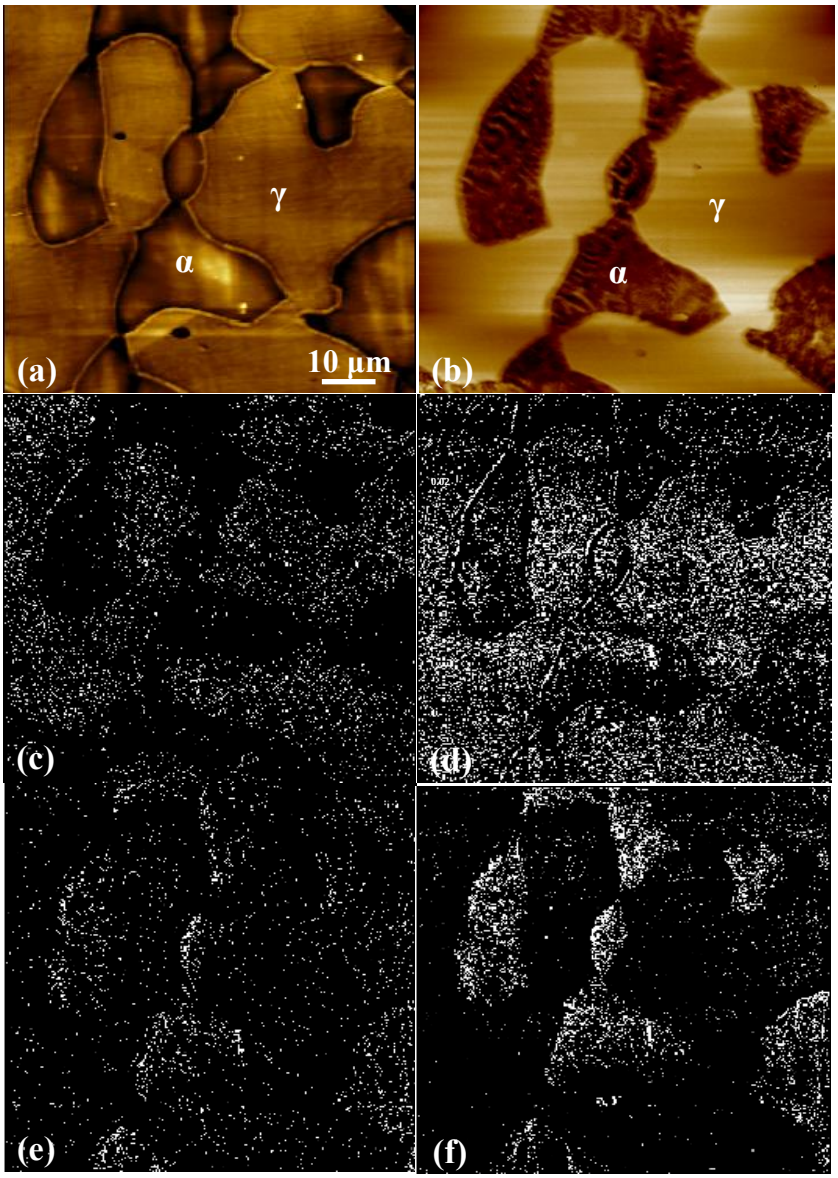

Fig.3. Depth profiles of chemical composition in oxide films formed on (a) austenite and (b) ferrite phases at 300°C; (d) austenite and (e) ferrite phases at 400°C; and the Cr/Fe atomic ratio at (c) 300°C and (f) 400°C.

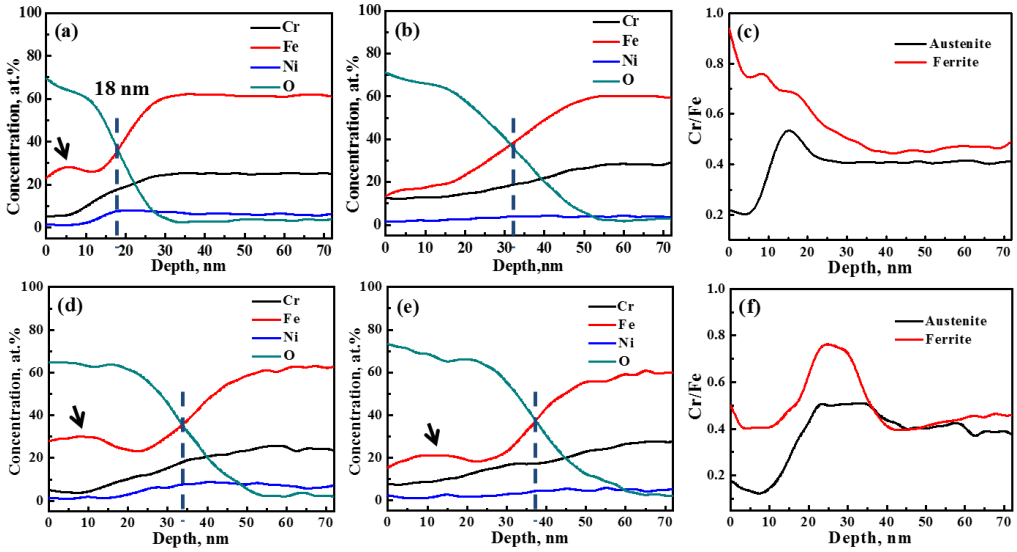

Fig.4. XPS spectra of Fe $2P_{2/3}$ of the oxidation film formed at the temperature of (a) 300°C and (b) 400 °C.

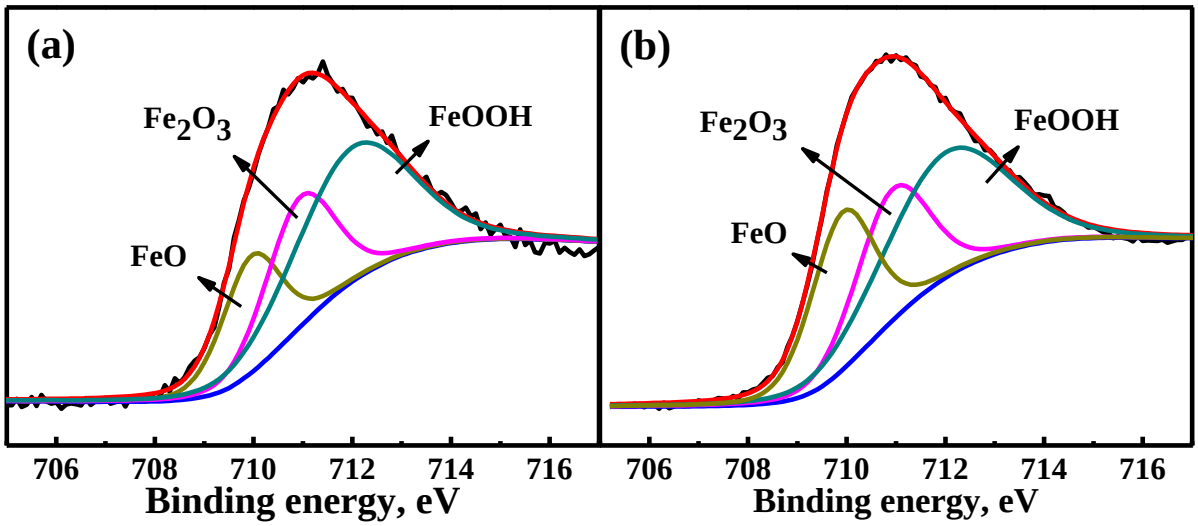

Fig.5. XPS spectra of Cr $2P_{2/3}$ of the oxidation film formed at the temperature of (a) 300°C and (b) 400 °C.

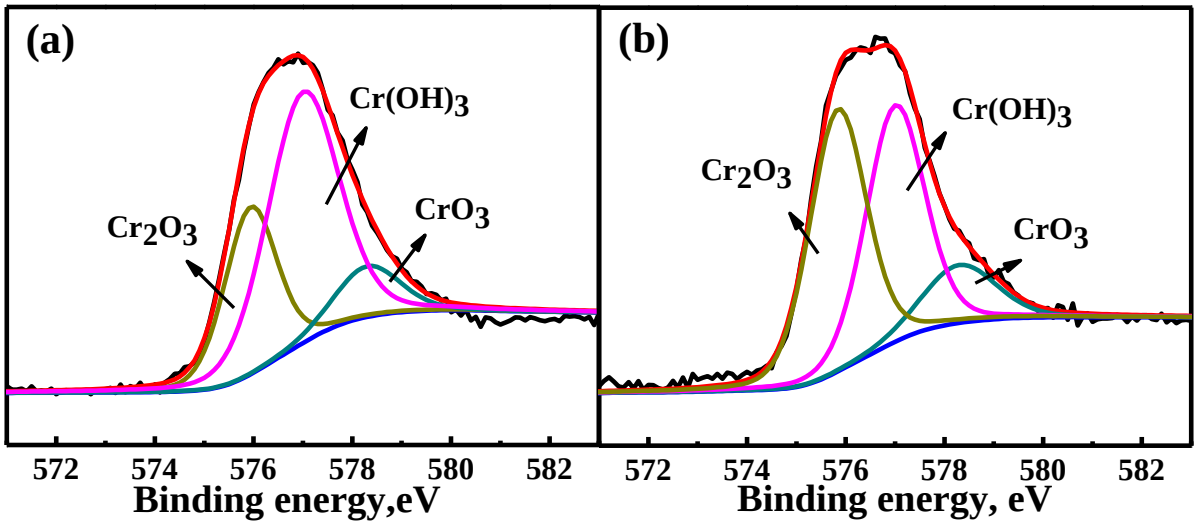

Fig.6. XPS spectra of Ni $2P_{2/3}$ of the oxidation film formed at the temperature of (a) 300°C and (b) 400 °C.

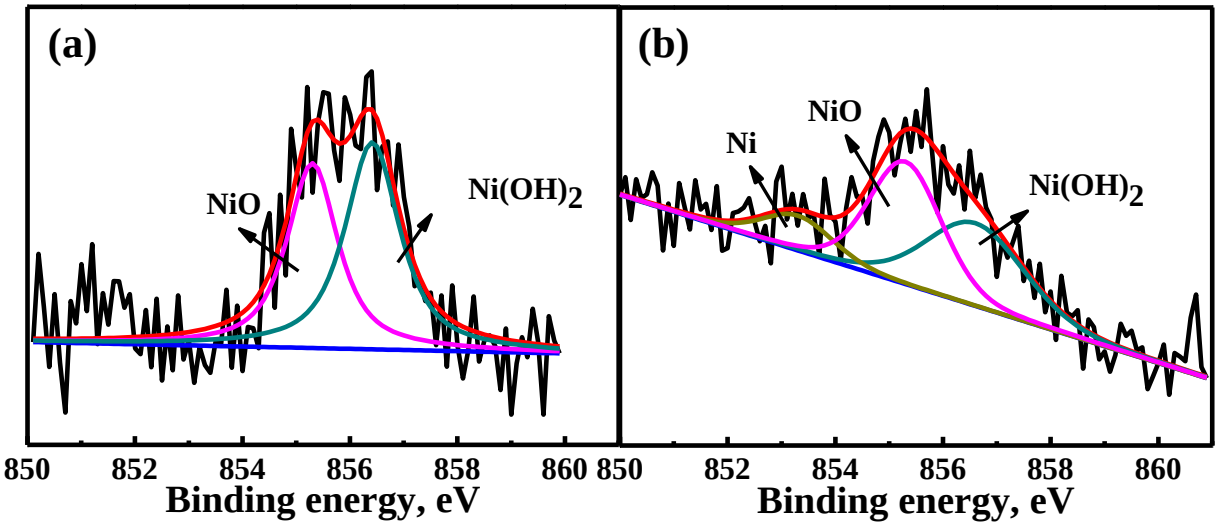

Fig.7. XPS spectra of Mo 3d of the oxidation film formed at the temperature of (a) 300°C and (b) 400 °C.

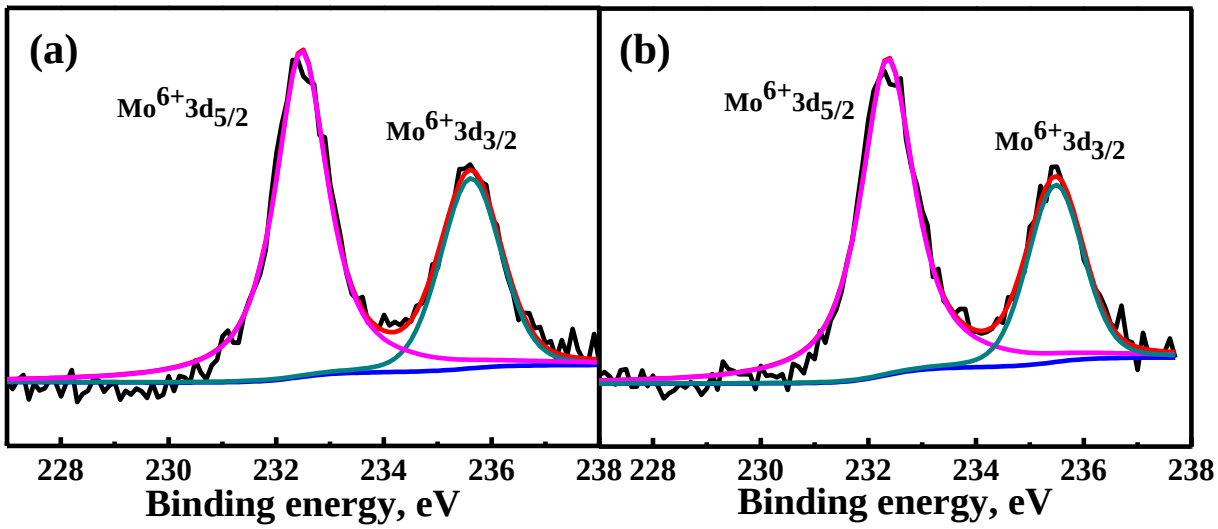

Fig.8. Schematic illustration of electronic structure of oxide films formed for (a) p-n type and (b) p-p type heterojunctions.